RSC Advances

PAPER

View Article Online
View Journal | View Issue

Check for updates

Cite this: *RSC Adv.*, 2022, **12**, 23437

Enhancing $K_2S_2O_8$ electrochemiluminescence based on silver nanoparticles and zinc metal–organic framework composite (AgNPs@ZnMOF) for the determination of L-cysteine†

Lina Wang,‡[a] Qi Wu,‡[a] Ru Yu,[a] Hongge Zhang,[b] Fei Nie *[a] and Wenyan Zhang*[a]

Received 30th June 2022
Accepted 2nd August 2022

DOI: 10.1039/d2ra04033f

rsc.li/rsc-advances

A silver nanoparticle-doped Zn(II) metal–organic framework composite (AgNPs@ZnMOF) was investigated as an electrochemiluminescence (ECL) signal enhancer for potassium persulfate. First, ZnMOF was prepared by a one-step hydrothermal method, and then AgNPs@ZnMOF composite was obtained by depositing AgNPs on the surface and interior of ZnMOF. After the AgNPs@ZnMOF composite was modified on the glass carbon electrode (GCE), the cathode luminescence of potassium persulfate on bare GCE was enhanced by 8 times. A dual amplification mechanism provided by Zn(II) and Ag nanoparticles in the AgNPs@ZnMOF composite has been validated by ECL spectra, fluorescence spectra, and electrochemical methods. The interaction between the sulfhydryl groups in L-cysteine (L-Cys) and AgNPs significantly affects the catalytic luminescence of the AgNPs@ZnMOF composite. Thus, a sensitive ECL method for the determination of L-Cys was developed based on the inhibition effect of L-Cys on the ECL signal within the linear range from 5.0 nM to 1.0 μM and the limit of detection was found to be 2 nM (S/N = 3). The established method has been successfully applied to the determination of L-Cys in human urine.

1. Introduction

Electrochemiluminescence (ECL) actually connects photochemistry and electrochemistry. Free radicals or free radical ions generated through the electrochemical reaction or the chemical reaction result in excited states species, which is displayed by the luminescent radiation.[1] The early ECL research was mostly in organic media based on an annihilation mechanism, because the majority of the luminescence reagents are very poorly soluble in water. The utilization of metal chelates, represented by $Ru(bpy)_3^{2+}$, as ECL luminescence reagents greatly improves the application prospect of the ECL method in water phase due to their solubility.[2] However, the narrow potential determination window of water brings new problems for the application of ECL in the aqueous phase, as it is not possible to obtain all the free radical species required to complete the ECL reaction in this medium by sequential potential switching between oxidation potential and reduction potential.[3] Therefore, coreactants are proposed to be used in ECL processes so that the ECL signal could be obtained in a single oxidation or reduction scan.[4]

Persulfate ($S_2O_8^{2-}$) is the most commonly used cathodic ECL coreactant. The reduction of $S_2O_8^{2-}$ on the cathode produces a strong oxidant of sulfate radical anion ($SO_4^{\bullet-}$) and assists in the subsequent cathodic ECL. It is worth mentioning that $SO_4^{\bullet-}$ can produce cathode luminescence with the help of dissolved oxygen in the solution, albeit very weakly.[5] Whether potassium persulfate is used as a coreactant or a luminescent signal substance, the luminescent signal is limited by the solubility of $S_2O_8^{2-}$ and the amount of $SO_4^{\bullet-}$ produced. Therefore, considerable efforts are devoted to the exploitation of coreactant accelerators that assist the conversion of $S_2O_8^{2-}$ into the $SO_4^{\bullet-}$ to output amplified ECL signals.[6,7]

Metal organic frameworks (MOFs), built up by metal ions and organic linkers, are a charming kind of porous crystalline material.[8,9] MOFs' applications in ECL are receiving more and more attention due to their brilliant features, such as large surface area, tailorable structure, high porosity, tunable size and versatile functionality.[10–12] Some MOFs have been used as co-reaction accelerators in ECL systems, such as IRMOF-3 (ref. 13) and UIO-66-NH_2,[14] mainly based on the organic ligand in MOFs, 2-amino terephthalic acid, which promotes the

---

[a] *Key Laboratory of Synthetic and Natural Functional Molecule Chemistry (Ministry of Education), College of Chemistry & Materials Science, Northwest University, Xi' an, 710069, PR China. E-mail: niefei@nwu.edu.cn; zhangwy@nwu.edu.cn*

[b] *Faculty of Chemistry and Chemical Engineering, Key Laboratory of Phytochemistry of Shaanxi Province, Baoji University of Arts and Sciences, Baoji, 721013, Shaanxi, PR China*

† Electronic supplementary information (ESI) available. See https://doi.org/10.1039/d2ra04033f

‡ These authors contributed equally to this work and should be considered co-first authors.

conversion of $S_2O_8^{2-}$ into the $SO_4^{\bullet-}$. The metal ions of MOFs, such as cupric ions and cobalt ions,[15,16] were also found to act as active centers to promote the production of $SO_4^{\bullet-}$. Due to the inherent poor electrical conductivity of most MOF materials, electrochemical polarization inevitably occurs by using MOF modified electrodes. One of the efficient ways to reduce the polarization is to decorate some noble metal nanomaterials on MOFs[17–20] to make the composite have good electrical conductivity and biocompatibility.

L-Cysteine (L-Cys) is a naturally occurring amino acid containing thiols, which plays a crucial role in biological systems. L-Cys can be secreted from the human body through urine in which the total L-Cys concentration of healthy individuals is in the 25–200 μM range.[21] Abnormal levels of L-Cys may occur for several clinical diseases, such as liver damage, cardiovascular disease and Alzheimer's disease.[22] Therefore, it will be an ideal diagnostic indicator for detecting serum or urine L-Cys in the patients at risk for cystine stone formation or with early renal injury of Diabetes Mellitus.[23,24] So far, a number of methodologies for detecting L-Cys have been developed, including fluorescence methods,[25] colorimetry,[26] electrochemical detection,[27] capillary electrophoresis[28] and high performance liquid chromatography.[29] ECL assays for determining L-Cys were also reported previously;[30,31] the determination of L-Cys by ECL methods has higher sensitivity compared to other methods. However, multiple luminescence reagents are usually needed and the modification steps are more complicated. Therefore, it is critical to develop fast, convenient and sensitive ECL methods for the quantitative analysis of L-Cys.

Herein, a 3D MOF material based on zinc salt was fabricated using a simple hydrothermal reaction method and AgNPs were loaded on/into it to make AgNPs@ZnMOF composites. The cathodic ECL signal of $K_2S_2O_8$ could be amplified about 8 times by using the AgNPs@ZnMOF modified GCE compared with bare GCE. Cyclic voltammetry, fluorescence spectroscopy and ECL spectroscopy were used to investigate the possible ECL enhancement mechanism and a dual amplification mechanism was proposed by the aid of the reduction-oxidation (REDOX) process of Zn(II) ions in ZnMOF and the electrocatalytic reduction process of AgNPs in the AgNPs@ZnMOF composite. As a kind of fluorescence emitter, ZnMOF was made into a composite with AgNPs and the composite was confirmed to act as catalysts for the potassium persulfate ECL reaction rather than the ECL emitter. This synergistic catalysis helped the reduction of $K_2S_2O_8$ and promoted the conversion of $S_2O_8^{2-}$ to $SO_4^{\bullet-}$. Interestingly, although other noble metal nanoparticles can also improve the conductivity of ZnMOF, they cannot effectively enhance the ECL of persulfate because they do not have the same electrocatalytic activity as AgNPs. This also indicates that the conductivity of MOF material contributes little to improving its ECL emission signal. In addition, AgNPs on the surface of the AgNPs@ZnMOF composite facilitate the binding of L-Cys due to their interaction with the sulfhydryl groups of L-Cys. Then, the catalytic ability of silver will be significantly affected thus inhibiting the ECL signal of the AgNPs@ZnMOF/$K_2S_2O_8$ system. Based on this, a very convenient ECL method was established for L-Cys determination using AgNPs@ZnMOF nanocomposite-modified glass carbon electrode (GCE) electrodes. The proposed method has good sensitivity and selectivity and can be used for the determination of L-Cys in urine samples directly.

2. Experiments

2.1. Reagents and chemicals

Potassium persulfate ($K_2S_2O_8$) was of analytical-reagent grade and purchased from Sigma Chemical Co. (St. Louis, MO, USA). 0.10 M phosphate buffered saline (PBS) at various pH values were prepared by mixing the different ratio stock solution of NaH_2PO_4 and Na_2HPO_4 which containing 0.10 M KCl as a supporting electrolyte. $ZnSO_4 \cdot 7H_2O$ and 2-(3,5-dicarboxylphenyl) -6-carboxyl-benzimidazole (H_3L) were purchased from Sinopharm Chemical Reagent Co. (Shanghai, China). Ascorbic acid (AA, 99%), uric acid (UA, 99%), glutathione (GSH, 98%), glucose (Glu), dopamine (DA) and L-Cysteine (L-Cys, 99%) were purchased from Aladdin Reagent Co. Ltd (Shanghai, China). L-glycine (L-Gly, 99%), L-proline (L-Pro, 99%), L-alanine (L-Ala, 99%) and L-Cystine (Cys–Cys, 99%) were provided by J&k Chemical Co. (Beijing, China). The urine samples were obtained from volunteers. All chemicals are analytical reagent grade without further purification. De-ionized water was used throughout.

2.2. Apparatus

The crystallinities of as-synthesized samples were characterized by powder X-ray diffraction (XRD) on a Bruker D-8 Advance diffractometer using Cu $K\alpha$ ($\lambda = 1.5406$ Å) radiation at a scanning rate of 6° $\min^{-1}$. The UV-vis spectra were measured with a UV-2600 UV/Vis spectrophotometer (Shimadzu, Japan). Fourier transform infrared (FT-IR) spectra were collected by using a Fourier transform infrared spectrophotometer (JASCO 6300). X-ray photoelectron spectroscopy (XPS) was carried out on a Thermo ESCALAB 250XI multifunctional imaging electron spectrometer using the binding energy of C as the internal standard. Scanning electron microscopy (SEM) image was obtained on a field-emission scanning electron microscopy (Zeiss Sigma 500). Transmission electron microscopy (TEM) images and energy dispersive X-ray spectroscopy (EDX) were obtained on a transmission electronmicroscopy (JEM-2100). The ECL measurements were recorded on an MPI-E multifunctional electrochemiluminescence analytical system (Remax Electronic Science & Technology Co. Ltd, Xi'an, China) with the voltage of the photomultiplier tube (PMT) setting at −800 V. The potential scanned from −1.6 to 0 V in the process of detection. A conventional three-electrode system was used with a glassy carbon electrode (GCE, 3 mm in diameter) used as the working electrode, a platinum wire (0.5 mm in diameter) as the counter electrode, and an Ag/AgCl (with saturated KCl solution) electrode as the reference electrode, respectively. The ECL spectra were obtained by collecting the ECL signals during cyclic potential scanning with filters of various wavelengths from 400 to 760 nm. Cyclic voltammetry (CV) and electrochemical impedance spectroscopy (EIS) measurements were carried out with a CHI-604D electrochemistry workstation (Shanghai Chenhua Instruments Co, China). EIS was carried out at open circuit potential in 0.1 mol L^{-1} KCl solution containing $K_3[Fe(CN)_6]/K_4[Fe(CN)_6]$ (5 mM, 1 : 1). The frequency range was selected as 0.01 Hz to 100 kHz, and potential amplitude was 5 mV.

2.3. Synthesis of ZnMOF

ZnMOF (CCDC number is 2 094 605) was synthesized according to previous method from our laboratory.[32] According to the synthesis protocol, $ZnSO_4 \cdot 7H_2O$ (0.06 mmol), H_3L (0.03 mmol), and DMF/H_2O (4.0 mL v/v, 3/1) (DMF = *N*,*N*-dimethylformamide) were mixed then heated at 95 °C for 72 h. Colorless block crystals were obtained in ~65.0% yield based on Zn. Elemental analysis found (%), C, 49.65; H, 3.96; N, 9.82. FTIR analysis (KBr, cm^{-1}, Fig. 1C), 3441(m), 2790(w), 1626(s), 1349(s), 1097(w), 1019(w), 784(m), 715(m), 611(w).

2.4. Preparation of the AgNPs@ZnMOF composite

ZnMOF (0.0318 mmol) and $AgNO_3$ (0.001 mmol) were added to a 10 mL mixed solvent of DMF/H_2O (3 : 1 v/v). After stirred for 2 h, 10 mL of 0.05 M $NaBH_4$ solution with same solvent was added to the above-mentioned mixed solution. The color of mixture turned black immediately, and the grey-black sample of AgNPs@ZnMOF was filtrated. The loading of Ag supported on AgNPs@ZnMOF material was dertermined as 1.3% (theoretical metal loading is 1.6%) by performing inductively coupled plasma mass spectrometry (ICP-MS).

2.5. Fabrication of the modified electrode

Before preparing the ECL sensor, the bare GCE was polished with 0.3 mm and 0.05 mm alumina slurry, successively, then the electrode was cleaned in ethanol and ultrapure water in turn to achieve a mirror-like surface. Afterward, 10.0 μL of AgNPs@ZnMOF dispersion (1 mg mL^{-1}) was dropped on the surface of polished GCE and dried at room temperature.

2.6. ECL measurement

The ECL signals and corresponding CV curves were recorded simultaneously at room temperature in 0.1 M air-saturated PBS (pH = 7.4) containing 0.1 M $K_2S_2O_8$ solution. For L-Cys ECL detection, the ECL signals were recorded under the same conditions when L-Cys solution with different concentrations was added (Scheme 1).

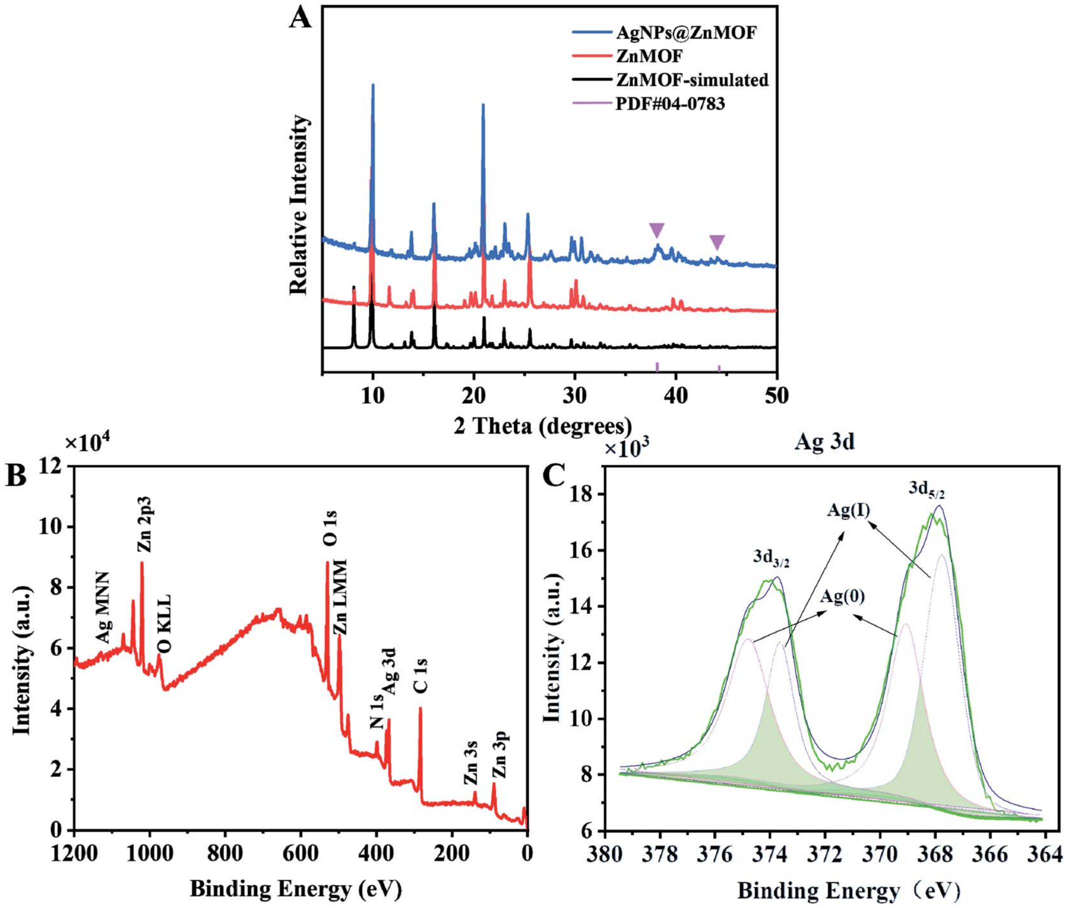

Fig. 1 (A) P-XRD patterns of ZnMOF and AgNPs@ZnMOF. (B and C) XPS survey spectra and XPS high-resolution spectra of Ag 3d of AgNPs@ZnMOF, respectively.

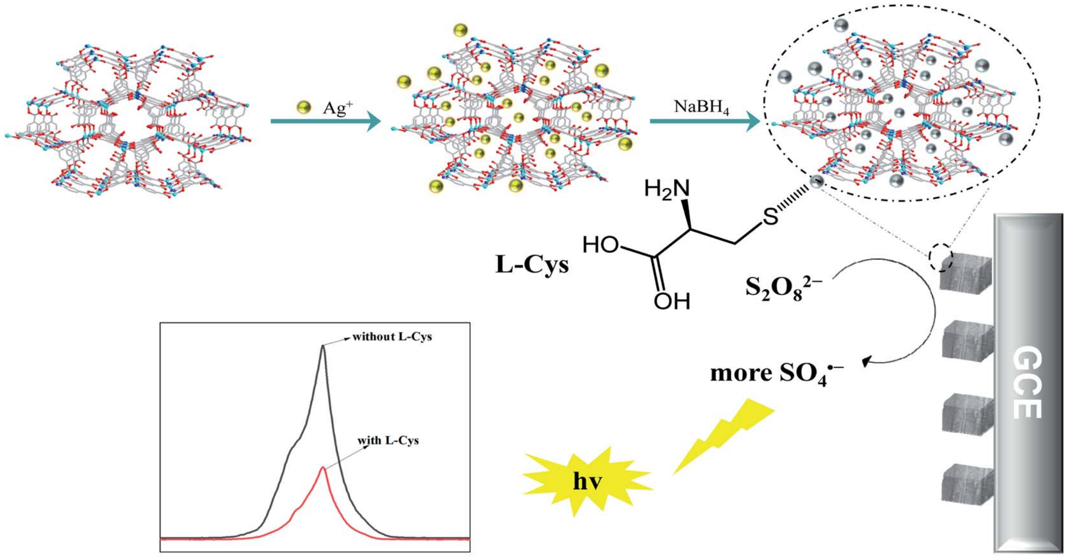

Scheme 1 Schematic illustration of the synthesis procedures of the AgNPs@ZnMOF and ECL detection mechanism of L-Cys.

3. Results and discussion

3.1. Characterization of ZnMOF and AgNPs@ZnMOF

The structures of ZnMOF and AgNPs@ZnMOF material were characterized by powder XRD (P-XRD) and compared with the simulated single crystal test data of ZnMOF (Fig. 1A). The PXRD data showed that the peak positions of the obtained crystalline samples of ZnMOF matched well with those simulated from the single-crystal data, showing the phase purity of the synthesized samples. The P-XRD patterns of ZnMOF and AgNPs@ZnMOF showed the characteristic reflections of the host matrix ZnMOF, which confirms the preservation of the ZnMOF intact structure after Ag(0) nanoparticle formation. Moreover, the P-XRD pattern of AgNPs@ZnMOF sample shows Bragg peaks at 38.12°, attributable to the (111) planes of the face-centered cubic (fcc) crystal structure of silver (JCPDS card number 04-0783).[33,34] The absorption peak at ~250 nm proved the presence of small AgNPs (Fig. S1)†.[35] The FTIR spectrum of AgNPs@ZnMOF is basically consistent with that of ZnMOF, implying that the ZnMOF remains intact after loading with AgNPs (Fig. S2).† Among them, the band corresponding to the stretching vibration at 3463 cm^{-1} is caused by water adsorbed on the material surface. 3071 cm^{-1} and 2874 cm^{-1} correspond to the stretching vibrations of –OH and C–H, respectively, and the peak observed at 1632 cm^{-1} is due to the stretching vibration of the carboxyl group on the ligand. 1361 cm^{-1} corresponds to the C–O vibration, and the bands observed between 600–1600 cm^{-1} and the bands observed between ~1600 cm^{-1} are due to benzene rings, including stretching vibrations at 1478 cm^{-1} (C=C) and deformation vibrations at 1014, 780, 720 and 610 cm^{-1} (C–H).

Among them, the band corresponding to the stretching vibration at 3463 cm^{-1} is caused by water adsorbed on the material surface. 3071 cm^{-1} and 2874 cm^{-1} correspond to the stretching vibrations of –OH and C–H, respectively, and the peak observed at 1632 cm^{-1} is due to the stretching vibration of the carboxyl group on the ligand. 1361 cm^{-1} corresponds to the C–O vibration, and the bands observed between 600–1600 cm^{-1} and the bands observed between ~1600 cm^{-1} are due to benzene rings, including stretching vibrations at 1478 cm^{-1} (C=C) and deformation vibrations at 1014, 780, 720 and 610 cm^{-1} (C–H).

The combined-state of Ag in AgNPs@ZnMOF was further investigated by XPS. The survey XPS spectrum for AgNPs@ZnMOF shows the co-existence of Ag, Zn, C, N and O (Fig. 1B, C and S3†). The oxidation state of Zn did not change during the reduction and the peak positions of C and N did not shift. Thus, it can be proved that the loading of AgNPs did not change the original framework structure of ZnMOF, and the oxidation states of each elements did not change (Fig. S3†). In the Ag 3d core level XPS spectra of the AgNPs@ZnMOF, signals with binding energies of 369.09 eV and 374.78 eV correspond to the 3d$_{5/2}$ and 3d$_{3/2}$ orbitals of Ag(0). The bind peaks of 367.74/373.64 eV are related to unreduced species and/or oxide species of Ag (Fig. 1C).

The morphology, size and composition of AgNPs@ZnMOF were investigated by SEM, SEM-EDX, TEM and HR-TEM analysis. Fig. S4A–4B† shows that the ZnMOF is in the shape of a rectangular block, mostly in the range of 50 μm, with some cracks on the surface, which may be caused by the collision during stirring and reduction. In addition, the EDX analysis of the randomly selected AgNPs@ZnMOF area could easily determine the boundaries of AgNPs@ZnMOF, according to the elemental distribution, and it was found that the Zn, Ag, N elements can overlap well, as well as Ag is uniformly distributed on the AgNPs@ZnMOF (Fig. S4C and D)†.

Fig. 2A shows the TEM images of AgNPs@ZnMOF, this image shows no agglomeration on the surface of ZnMOF crystals to form large size silver clumps, but the AgNPs at the edges of the MOF are slightly larger than inside. As shown in Fig. 2B, the lattice stripe of AgNPs@ZnMOF was clearly visible with a *d*-spacing of 0.2349 nm, confirming the formation of Ag (111)

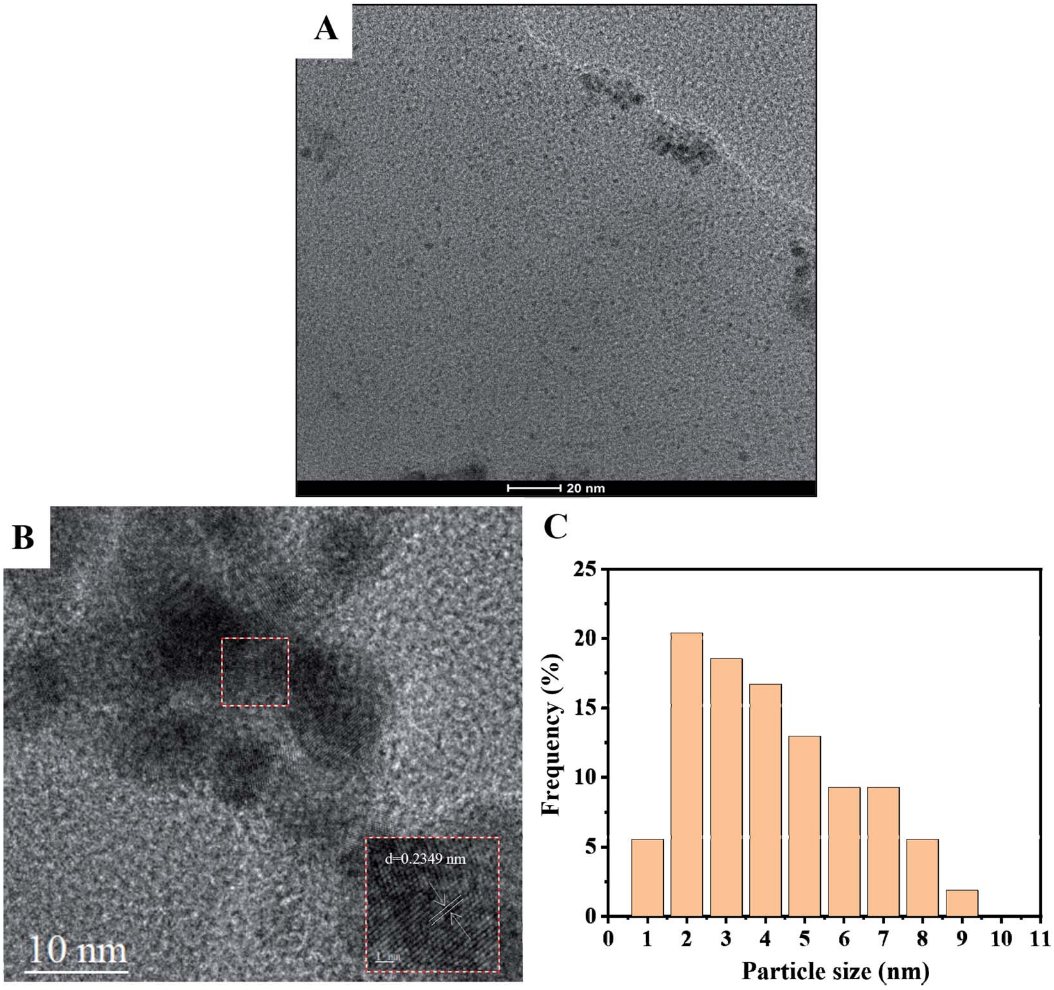

Fig. 2 (A) TEM image of AgNPs@ZnMOF. (B) HR-TEM image of AgNPs@ZnMOF. (C) Associated particle size histogram.

planes.[36] The average particle size of Ag(0) NPs inside the AgNPs@ZnMOF catalyst was 2.81 ± 0.22 nm based on the particle size analysis and calculated for 100 non-contact particles (Fig. 2C).

3.2. ECL behavior of the modified electrodes

In order to better analyze the function of each component in the AgNPs@ZnMOF composite, electrochemical and ECL behaviors of ZnMOF, AgNPs and AgNPs@ZnMOF modified GCE were comparatively studied in PBS solution (pH = 7.4) containing 0.1 M $K_2S_2O_8$. As shown in Fig. 3A, a reduction peak at −0.9 V was observed on GCE, which corresponding to the reduction of $S_2O_8{}^{2-}$ and a weak ECL signal was obtained at the same time (Fig. 3B). On the AgNPs modified electrode, it was observed that the luminescence signal of $S_2O_8{}^{2-}$ was slightly stronger than that of GCE electrode, and the reduction current was enhanced and the reduction potential shifted positively to about −0.7 V. In contrast, when ZnMOF was used to modify the electrode, in addition to the reduction peak of $S_2O_8{}^{2-}$ (slightly negative to −1.0 V), a pair of redox peaks were occurred at −0.98 and −1.2 V which might relate to ZnMOF. The electrochemical behavior of ZnMOF modified electrode in PBS solution (0.10 M, pH 7.4) was investigated (Fig. S5A),† and a pair of redox peaks (at −0.98 V and −1.2 V) were found to be completely consistent with the results obtained in $K_2S_2O_8$ solution, which is also close to the potential of Zn(II) redox peaks on a ZnO nanomaterial modified electrode.[37] The redox peak current increased linearly with the CV scan rate (ν) from 10 to 200 mV (Fig. S5B).† It is also confirmed that ZnMOF on the electrode surface dominates the electrochemical process. The redox process of ZnMOF also contributed to the ECL reaction of $S_2O_8{}^{2-}$, and the ECL signal was enhanced compared with that of GCE. Similarly, three electrochemical peaks were observed on the AgNPs@ZnMOF composite modified electrode. However, the reduction peak of $S_2O_8{}^{2-}$ shifted positively to about 0.6 V, while the potential of the other redox peaks was basically the same as ZnMOF and the current intensity increased significantly. Differently, the reduction peak of AgNPs@ZnMOF shifted positively (−1.1 V) in PBS solution compared to ZnMOF (Fig. S5A)†, illustrating that the addition of AgNPs makes the reduction of ZnMOF easier and promotes its reduction process. The ECL intensity of AgNPs@ZnMOF composite is higher than GCE nearly 8-folds. This demonstrated that ZnMOF and AgNPs could play

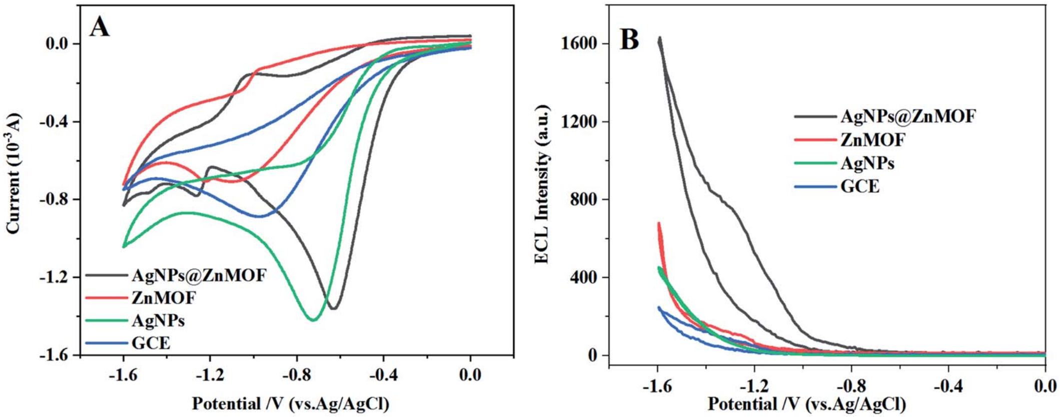

Fig. 3 (A) CV curves and (B) ECL responses of GCE, AgNPs, ZnMOF and AgNPs@ZnMOF in the 0.10 M $K_2S_2O_8$ solution, respectively.

a synergistic effect, making the AgNPs@ZnMOF composite a more effective catalyst for amplifying the ECL of $K_2S_2O_8$.

In addition to AgNPs, the effects of the composites of several other noble metal nanoparticles and ZnMOF on the ECL of $K_2S_2O_8$ were also compared. The EIS experiments characterized in the $[Fe(CN)_6]^{3-/4-}$ solution showed that charge transfer resistance (R_{ct}) of ZnMOF can be effectively reduced by several noble metal nanoparticles (Fig. S6).† However, the enhancement effect on $S_2O_8^{2-}$ ECL was not obvious on other composite modified electrodes except AgNPs@ZnMOF (Fig. S7).† Furthermore, the positive shifting reduction peak of $S_2O_8^{2-}$ was observed only on AgNPs@ZnMOF modified GCE (Fig. S8).† This also validated that AgNPs has a more significant catalytic effect on the electroreduction process of $S_2O_8^{2-}$ to enhance the ECL signal,[38] compared with the noble metal nanomaterials which only improve the conductivity of ZnMOF.

As a typical d^{10} metal complex, ZnMOFs often exhibit luminescent activity provided by their ligands. The ZnMOF prepared in this work also has fluorescence activity[32] and generates an emission signal at 371 nm when the fluorescence excitation wavelength is 320 nm (Fig. 4A). Compared the fluorescence spectrum of ZnMOF with that of the composite loaded with AgNPs, no obvious shift was observed, indicating that the fluorescence characteristics of ZnMOF determined by its ligands were not affected by loading with AgNPs. Nevertheless, an obvious red-shift has occurred by comparing the fluorescence spectra of AgNPs@ZnMOF composite with the ECL spectrum of AgNPs@ZnMOF/$K_2S_2O_8$ ECL system (Fig. 4B), which suggested that the AgNPs@ZnMOF composite is unlikely to be the ECL emitter, and the ECL signal should come from $S_2O_8^{2-}$ in the system. The wavelengths of the two ECL peaks are basically consistent with that of the singlet oxygen ($^1(O_2)_2{}^*$) generated in the reduction of $S_2O_8^{2-}$ reported in the literature.[15]

According to the results described above, we speculate that the ECL mechanism of the AgNPs@ZnMOF/$K_2S_2O_8$ system. When the CV potential was scanned to −0.6 V, the $S_2O_8^{2-}$ was reduced to $SO_4^{\bullet-}$ at the cathode with the help of AgNPs. As the potential continued to scan to −1.2 V, ZnMOF on the electrode surface began to be electrically reduced, and the resulting reduction product changed $K_2S_2O_8$ into $SO_4^{\bullet-}$. Due to the synergistic effect of AgNPs and ZnMOF in the composite, a large amount of $SO_4^{\bullet-}$ was produced and the ECL signal enhanced significantly.

3.3. The ECL determination of L-Cys

After adding L-Cys to the AgNPs@ZnMOF/$K_2S_2O_8$ system, the ECL signal is decreased, which may due to forming the Ag–S bonds between L-Cys with AgNPs because the high affinity of the

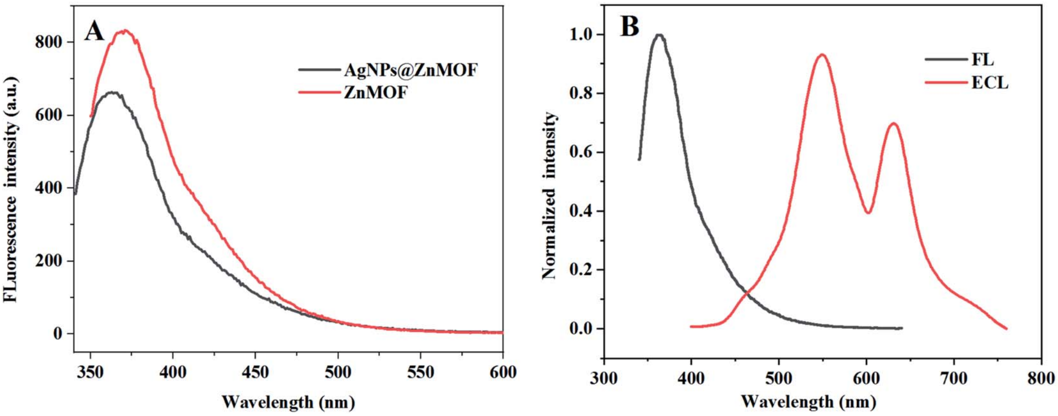

Fig. 4 (A) FL spectra ($\lambda_{ex} = 320$ nm) of ZnMOF and AgNPs@ZnMOF; (B) ECL spectrum and FL spectrum of AgNPs@ZnMOF.

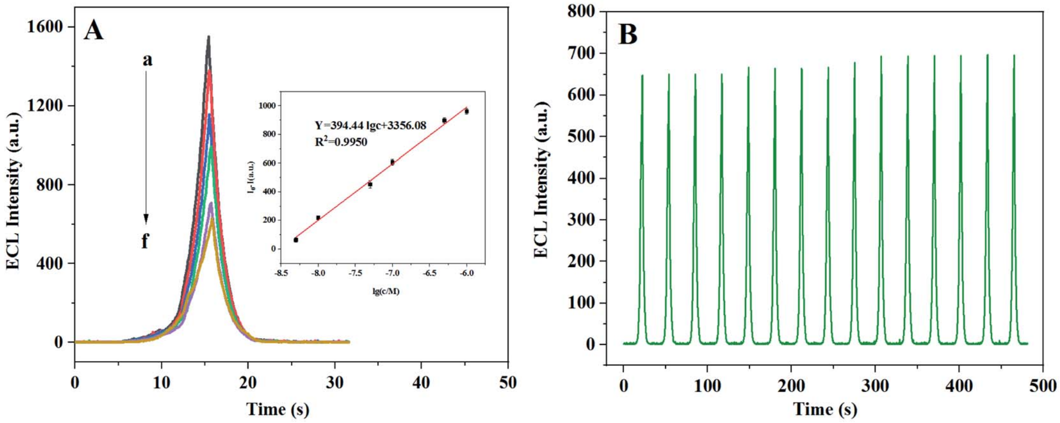

Fig. 5 ECL responses of the AgNPs@ZnMOF enhanced $K_2S_2O_8$ system for different concentrations of L-Cys (from a to f, 5.0×10^{-9}, 1.0×10^{-8}, 5.0×10^{-8}, 1.0×10^{-7}, 5.0×10^{-7}, 1.0×10^{-6} M), inset showed the calibration curve for L-Cys detection. (B) Stability of the ECL detection.

Table 1 Comparison of different methods for L-Cys detection

Method	Probes	Linear range M	Detection limit M	Ref.
Colorimetry	Fe_3O_4 nanofibers	2.0×10^{-6}–1.0×10^{-5}	2.8×10^{-8}	40
Fluorescence	N-H-CQDs	0–1.0×10^{-4}	2.42×10^{-7}	41
Fluorescence	Ca-MOFs/Pb^{2+}	5.0×10^{-8}–4.0×10^{-5}	1.5×10^{-8}	25
Photoelectrochemical	CuO–Cu_2O	2.0×10^{-7}–1.0×10^{-5}	5.0×10^{-8}	42
Electrochemistry	PdNPs	5.0×10^{-7}–1.0×10^{-5}	1.5×10^{-7}	43
ECL	CdTe QDs	1.3×10^{-6}–3.5×10^{-5}	8.7×10^{-7}	44
ECL	ZnO/MoS_2	1.0×10^{-8}–1.0×10^{-6}	6.5×10^{-9}	31
ECL	AgNPs@ZnMOF	5.0×10^{-9}–1.0×10^{-6}	2×10^{-9}	This work

thiol group with silver.[39] On this basis, an ECL method for the determination of L-Cys was proposed. Several factors that might affect the performance of ECL analysis were optimized including pH and the concentration of potassium persulfate (Fig. S9).† Under the optimized conditions, an acceptable linear connection between the ECL signal and the logarithm of the L-Cys concentration (log C L-Cys) was obtained in the range of 5.0 nM to 1.0 μM and the detection limit was determined of 2 nM (S/N = 3) (Fig. 5A). Compared with other optical methods for L-Cys determination reported in the literature, the ECL method described here has a lower detection limit and a wider linear detection range (Table 1).

3.4. Selectivity and stability of the ECL detection

To test the selectivity of this ECL method, the effect of some substances on L-Cys determination was investigated at the same concentration level as L-Cys (1.0 μM), such as DA, AA, Glu, UA, GSH, L-Gly, L-Pro, L-Ala and Cys–Cys (Fig. S10).† Compared with blank signal, the interference of other substances was not significant except for GSH. Considering that the content of GSH in the actual biological samples is often very low and much lower than the level of L-Cys, the interference study on the lower concentration of GSH (1.0×10^{-8} M) was carried out again, and the results showed that the influence of GSH on the dermination of L-Cys could be almost negligible. The ECL intensity of the sample mixed with L-Cys and other substances at the same concentration (1.0 μM, GSH = 1.0×10^{-8} M) was not significantly different from that of the solution with only L-Cys, showing that this method has a good anti-interference ability. Stable ECL signals can be obtained by 15 consecutive measurements (Fig. 5B), with a relative standard deviation of 2%, demonstrating a good stability of the method.

Table 2 Determination of L-Cys in human urine samples (*n* = 3)

Sample	ECL method μM	Added/μM	Found/μM	Recovery/%	RSD/%
1	0.31	0.10	0.40	98	3.7
	0.35	0.20	0.53	96	2.6
	0.38	0.50	0.91	103	4.3
2	0.40	0.10	0.48	96	5.0
	0.48	0.20	0.66	97	4.6
	0.46	0.50	1.0	104	3.9

3.5. Sample analysis

The proposed method was used to analyze L-Cys in human urine. The urine samples were centrifuged and diluted 100-folds with 0.1 M PBS (pH = 7.4) and then 0.1 M $K_2S_2O_8$ was added to the diluted urine sample. The L-Cys was detected with AgNPs@ZnMOF modified GCE directly. The results in Table 2 showed that L-Cys levels in the urine samples were consistent with normal levels in healthy people.[21] The spiked samples were determined with recoveries in the range of 96%–104% showing that the designed method could be successfully applied for the quantification of the L-Cys in human urine samples with acceptable accuracy.

4. Conclusion

In summary, ZnMOF was synthesized by a simple hydrothermal method and loaded with Ag nanoparticles. The obtained AgNPs@ZnMOF composite served as an electrode modified material and assisted potassium persulfate to produce a cathode ECL signal, which was 8 times stronger than the ECL signal on the bare electrode. In the composite, a dual ECL amplification mechanism is derived from the enhanced conductivity of MOF, as well as the electroreduction catalytic effect of potassium persulfate by AgNPs and the REDOX process of ZnMOF itself, which also sensitizes ECL. An ECL method for detection of L-Cys was established and the proposed method displayed good selectivity and has been applied to detect L-Cys in urine with satisfactory results. It provides ideas for solving the problem of electroactivity of MOF in ECL analysis and improving the sensitivity of ECL method.

Ethical statement

The authors state that all experiments were performed in compliance with the relevant laws and institutional guidelines. The institutional committee of the Northwest University approved the experiment. The authors also state that informed consent was obtained for any experimentation with human subjects and the human serum samples useds in this study didn't have any identifying information about all the participants that provided written informed consent.

Conflicts of interest

There are no conflicts to declare.

Acknowledgements

The authors are grateful for the financial support from the National Natural Science Foundation of China (grant no.21531007), the Phytochemistry Key Laboratory of Shaanxi Province (grant no.18JS007) and the Xi'an Science and Technology Project (XA2020-CXRCFW-0021), the Shaanxi Provincial Natural Science Basic Research Program (2019JM-590), and the Open Foundation of Key Laboratory of Synthetic and Natural Functional Molecular Chemistry of Ministry of Education (KLSNFM2020001).

References

1 L. Li, Y. Chen and J. J. Zhu, Recent Advances in Electrochemiluminescence Analysis, *Anal. Chem.*, 2017, **89**(1), 358–371.

2 H. J. Li, S. Han, L. Z. Hu and G.-B. Xu, Progress in $Ru(bpy)_3^{2+}$ Electrogenerated Chemiluminescence, *Chinese J. Anal. Chem.*, 2009, **37**(11), 1557–1565.

3 C. Ma, Y. Cao, X. Gou and J. J. Zhu, Recent Progress in Electrochemiluminescence Sensing and Imaging, *Anal. Chem.*, 2020, **92**(1), 431–454.

4 J. Ludvík, DC-electrochemiluminescence (ECL with a coreactant)—principle and applications in organic chemistry, *J. Solid State Electrochem.*, 2011, **15**(10), 2065.

5 O. V. Reshetnyak and E. P. Koval'chuk, A possible scheme of electrochemiluminescence generation on platinum cathodes in aqueous solutions of peroxydisulfates, *Electrochim. Acta*, 1998, **43**(5), 465–469.

6 X. Song, X. Li, D. Wei, R. Feng, T. Yan, Y. Wang, X. Ren, B. Du, H. Ma and Q. Wei, CuS as co-reaction accelerator in PTCA-$K_2S_2O_8$ system for enhancing electrochemiluminescence behavior of PTCA and its application in detection of amyloid-β protein, *Biosens. Bioelectron.*, 2019, **126**, 222–229.

7 W. J. Zeng, N. Liao, Y. M. Lei, J. Zhao, Y. Q. Chai, R. Yuan and Y. Zhuo, Hemin as electrochemically regenerable co-reaction accelerator for construction of an ultrasensitive PTCA-based electrochemiluminescent aptasensor, *Biosens. Bioelectron.*, 2018, **100**, 490–496.

8 D. I. Osman, S. M. El-Sheikh, S. M. Sheta, O. I. Ali, A. M. Salem, W. G. Shousha, S. F. El-Khamisy and S. M. Shawky, Nucleic acids biosensors based on metal-organic framework (MOF): Paving the way to clinical laboratory diagnosis, *Biosens. Bioelectron.*, 2019, **141**, 111451.

9 S. Wang, M. Wang, C. Li, H. Li, C. Ge, X. Zhang and Y. Jin, A highly sensitive and stable electrochemiluminescence immunosensor for alpha-fetoprotein detection based on luminol-AgNPs@Co/Ni-MOF nanosheet microflowers, *Sens. Actuators, B*, 2020, **311**, 127919.

10 J. Zhou, Y. Li, W. Wang, X. Tan, Z. Lu and H. Han, Metal-organic frameworks-based sensitive electrochemiluminescence biosensing, *Biosens. Bioelectron.*, 2020, **164**, 112332.

11 D. Du, J. Shu, M. Guo, M. A. Haghighatbin, D. Yang, Z. Bian and H. Cui, Potential-Resolved Differential Electrochemiluminescence Immunosensor for Cardiac Troponin I Based on MOF-5-Wrapped CdS Quantum Dot Nanoluminophores, *Anal. Chem.*, 2020, **92**(20), 14113–14121.

12 Y. Wang, Y. Zhang, H. Sha, X. Xiong and N. Jia, Design and Biosensing of a Ratiometric Electrochemiluminescence Resonance Energy Transfer Aptasensor between a g-C_3N_4 Nanosheet and Ru@MOF for Amyloid-β Protein, *ACS Appl. Mater. Interfaces*, 2019, **11**(40), 36299–36306.

13 X. Yang, Y. Q. Yu, L. Z. Peng, Y. M. Lei, Y. Q. Chai, R. Yuan and Y. Zhuo, Strong Electrochemiluminescence from MOF Accelerator Enriched Quantum Dots for Enhanced Sensing of Trace cTnI, *Anal. Chem.*, 2018, **90**(6), 3995–4002.

14 Q. Fang, Z. Lin, F. Lu, Y. Chen, X. Huang and W. Gao, A sensitive electrochemiluminescence immunosensor for the detection of PSA based on CdWS nanocrystals and Ag^+@UIO-66-NH_2 as a novel coreaction accelerator, *Electrochim. Acta*, 2019, **302**, 207–215.

15 T. Tang, Z. Hao, H. Yang, F. Nie and W. Zhang, A highly enhanced electrochemiluminescence system based on

a novel Cu-MOF and its application in the determination of ferrous ion, *J. Electroanal. Chem.*, 2020, **856**, 113498.

16 X. Song, X. Shao, L. Dai, D. Fan, X. Ren, X. Sun, C. Luo and Q. Wei, Triple Amplification of 3,4,9,10-Perylenetetracarboxylic Acid by Co^{2+}-Based Metal-Organic Frameworks and Silver–Cysteine and Its Potential Application for Ultrasensitive Assay of Procalcitonin, *ACS Appl. Mater. Interfaces*, 2020, **12**(8), 9098–9106.

17 L. Li, Y. Zhao, Q. Wang, Z. Y. Liu, X. G. Wang, E. C. Yang and X. J. Zhao, Boosting photocatalytic hydrogen production activity by a microporous CuII-MOF nanoribbon decorated with Pt nanoparticles, *Inorg. Chem. Front.*, 2021, **8**(14), 3556–3565.

18 R. Yan, Y. Zhao, H. Yang, X. J. Kang, C. Wang, L. L. Wen and Z. D. Lu, Ultrasmall Au Nanoparticles Embedded in 2D Mixed-Ligand Metal-Organic Framework Nanosheets Exhibiting Highly Efficient and Size-Selective Catalysis, *Adv. Funct. Mater.*, 2018, **28**(34), 1802021.

19 J. Dong, D. Zhang, C. Li, T. Bai, H. Jin and Z. Suo, A sensitive electrochemical sensor based on PtNPs@Cu-MOF signal probe and DNA walker signal amplification for Pb^{2+} detection, *Bioelectrochemistry*, 2022, **146**, 108134.

20 Z. Mu, J. Tian, J. Wang, J. Zhou and L. Bai, A new electrochemical aptasensor for ultrasensitive detection of endotoxin using Fe-MOF and AgNPs decorated P-N-CNTs as signal enhanced indicator, *Appl. Surf. Sci.*, 2022, **573**, 151601.

21 R. Prasetia, S. Fuangswasdi and F. Unob, Silver nanoparticle-supported hydroxyapatite as a material for visual detection of urinary cysteine, *Anal. Methods*, 2019, **11**(22), 2888–2894.

22 M. Maruthupandi and N. Vasimalai, Nanomolar detection of L-cysteine and Cu^{2+} ions based on Trehalose capped silver nanoparticles, *Microchem. J.*, 2021, **161**, 105782.

23 R. Siener, N. Bitterlich, H. Birwé and A. Hesse, The Impact of Diet on Urinary Risk Factors for Cystine Stone Formation, *Nutrients*, 2021, **13**(2), 528.

24 A. V. Dnyanmote, S. P. Sawant, E. A. Lock, J. R. Latendresse, A. A. Warbritton and H. M. Mehendale, Calpastatin overexpression prevents progression of S-1,2-dichlorovinyl-l-cysteine (DCVC)-initiated acute renal injury and renal failure (ARF) in diabetes, *Toxicol. Appl. Pharmacol.*, 2006, **215**(2), 146–157.

25 B. Yang, X. Li, J. An, H. Zhang, M. Liu, Y. Cheng, B. Ding and Y. Li, Designing an "Off–On" Fluorescence Sensor Based on Cluster-Based CaII-Metal–Organic Frameworks for Detection of l-Cysteine in Biological Fluids, *Langmuir*, 2019, **35**(30), 9885–9895.

26 S. Chen, M. Chi, Y. Zhu, M. Gao, C. Wang and X. Lu, A Facile synthesis of superparamagnetic Fe_3O_4 nanofibers with superior peroxidase-like catalytic activity for sensitive colorimetric detection of l-cysteine, *Appl. Surf. Sci.*, 2018, **440**, 237–244.

27 K. Atacan, $CuFe_2O_4$/reduced graphene oxide nanocomposite decorated with gold nanoparticles as a new electrochemical sensor material for L-cysteine detection, *J. Alloys Compd.*, 2019, **791**, 391–401.

28 A. V. Ivanov, P. O. Bulgakova, E. D. Virus, M. P. Kruglova, V. V. e. Alexandrin, V. A. Gadieva, B. P. Luzyanin, N. E. e. Kushlinskii, A. N. Fedoseev and A. A. Kubatiev, Capillary electrophoresis coupled with chloroform-acetonitrile extraction for rapid and highly selective determination of cysteine and homocysteine levels in human blood plasma and urine, *Electrophoresis*, 2017, **38**(20), 2646–2653.

29 A. Kamińska, P. Olejarz, K. Borowczyk, R. Głowacki and G. Chwatko, Simultaneous determination of total homocysteine, cysteine, glutathione, and N-acetylcysteine in brain homogenates by HPLC, *J. Sep. Sci.*, 2018, **41**(16), 3241–3249.

30 J. Wu, P. Ran, S. Zhu, F. Mo, C. Wang and Y. Fu, A highly sensitive electrochemiluminescence sensor for the detection of l-cysteine based on the rhombus-shaped rubrene microsheets and platinum nanoparticles, *Sens. Actuators, B*, 2019, **278**, 97–102.

31 K. Tian, Y. Zhang, S. Zhang and Y. Dong, Electrogenerated Chemiluminescence of ZnO/MoS_2 Nanocomposite and Its Application for Cysteine Detection, *J. Electrochem. Soc.*, 2019, **166**(12), H527–H533.

32 Q. Wu, X. L. Yang, Z. Y. Ding, X. Y. Meng, W. Y. Zhang, Y. T. Yan and Y. Y. Wang, A multi-functional two-dimensional Zn (ii)-organic framework for selective carbon dioxide adsorption, sensing of nitrobenzene and $Cr_2O_7^{2-}$, *CrystEngComm*, 2021, **23**(43), 7643–7649.

33 I. Gumus, Y. Karataş and M. Gülcan, Silver nanoparticles stabilized by a metal–organic framework (MIL-101 (Cr)) as an efficient catalyst for imine production from the dehydrogenative coupling of alcohols and amines, *Catal. Sci. Technol.*, 2020, **10**(15), 4990–4999.

34 A. M. Awwad, N. M. Salem and A. O. Abdeen, Green synthesis of silver nanoparticles using carob leaf extract and its antibacterial activity, *J. Indian Chem.*, 2013, **4**(1), 1–6.

35 M. M. Alvarez, J. T. Khoury, T. G. Schaaff, M. N. Shafigullin, I. Vezmar and R. L. Whetten, Optical absorption spectra of nanocrystal gold molecules, *J. Phys. Chem. B*, 1997, **101**(19), 3706–3712.

36 R. Chen, N. T. Nuhfer, L. Moussa, H. R. Morris and P. M. Whitmore, Silver sulfide nanoparticle assembly obtained by reacting an assembled silver nanoparticle template with hydrogen sulfide gas, *Nanotechnology*, 2008, **19**(45), 455604.

37 R. Yuan, L. Ding, F. You, Z. Wen, Q. Liu and K. B. Wang, N co-doped graphene synergistic catalyzed ZnO quantum dots with amplified cathodic electrochemiluminescence for fabricating microcystin-LR aptasensor, *Sens. Actuators, B*, 2021, **349**, 130795.

38 Y. Y. Zhang, Q. M. Feng, J. J. Xu and H. Y. Chen, Silver Nanoclusters for High-Efficiency Quenching of CdS Nanocrystal Electrochemiluminescence and Sensitive Detection of microRNA, *ACS Appl. Mater. Interfaces*, 2015, **7**(47), 26307–26314.

39 Y. Ma, H. Xu, X. Shen and Y. Pang, Facile photoreductive synthesis of silver nanoparticles for antimicrobial studies, *Adv. Powder Technol.*, 2021, **32**(6), 2116–2121.

40 B. Thirumalraj, N. Dhenadhayalan, S. M. Chen, Y. J. Liu, T. W. Chen, P. H. Liang and K. C. Lin, Highly sensitive fluorogenic sensing of L-Cysteine in live cells using gelatin-stabilized gold nanoparticles decorated graphene nanosheets, *Sens. Actuators, B*, 2018, **259**, 339–346.

41 X. Jiang, J. Huang, T. Chen, Q. Zhao, F. Xu and X. Zhang, Synthesis of hemicellulose/deep eutectic solvent based carbon quantum dots for ultrasensitive detection of Ag^+ and L-cysteine with "off-on" pattern, *Int. J. Biol. Macromol.*, 2020, **153**, 412–420.

42 Y. Zhu, Z. Xu, K. Yan, H. Zhao and J. Zhang, One-Step Synthesis of $CuO–Cu_2O$ Heterojunction by Flame Spray Pyrolysis for Cathodic Photoelectrochemical Sensing of l-Cysteine, *ACS Appl. Mater. Interfaces*, 2017, **9**(46), 40452–40460.

43 N. Yusoff, P. Rameshkumar, M. Noor and N. M. Huang, Amperometric determination of L-cysteine using a glassy carbon electrode modified with palladium nanoparticles grown on reduced graphene oxide in a Nafion matrix, *Microchim. Acta*, 2018, **185**(4), 1–10.

44 Y. Ji, F. Dai and B. Zhou, Developing a julolidine-fluorescein-based hybrid as a highly sensitive fluorescent probe for sensing and bioimaging cysteine in living cells, *Talanta*, 2019, **197**, 631–637.